

SOSR: Source-Free Image Super-Resolution with Wavelet Augmentation Transformer

Yuang Ai^{1,4}, Xiaoqiang Zhou^{1,3}, Huaibo Huang^{1,2}, Lei Zhang⁵, Ran He^{1,2,6}

¹ MAIS & CRIPAC, Institute of Automation, Chinese Academy of Sciences, China

² School of Artificial Intelligence, University of Chinese Academy of Sciences, China

³ University of Science and Technology of China ⁴ Beijing Institute of Technology

⁵ Department of Computing, The Hong Kong Polytechnic University

⁶ School of Information Science and Technology, ShanghaiTech University, China

aiyuang2023@ia.ac.cn, xq525@mail.ustc.edu.cn,

huaibo.huang@cripac.ia.ac.cn, cslzhang@comp.polyu.edu.hk, rhe@nlpr.ia.ac.cn

Abstract

Real-world images taken by different cameras with different degradation kernels often result in a cross-device domain gap in image super-resolution. A prevalent attempt to this issue is unsupervised domain adaptation (UDA) that needs to access source data. Considering privacy policies or transmission restrictions of data in many practical applications, we propose a *Source-free image Super-Resolution framework (SOSR)* to address this issue, i.e., adapt a model pre-trained on labeled source data to a target domain with only unlabeled target data. SOSR leverages the source model to generate refined pseudo-labels for teacher-student learning. To better utilize the pseudo-labels, this paper proposes a novel wavelet-based augmentation method, named *Wavelet Augmentation Transformer (WAT)*, which can be flexibly incorporated with existing networks, to implicitly produce useful augmented data. WAT learns low-frequency information of varying levels across diverse samples, which is aggregated efficiently via deformable attention. Furthermore, an uncertainty-aware self-training mechanism is proposed to improve the accuracy of pseudo-labels, with inaccurate predictions being rectified by uncertainty estimation. To acquire better SR results and avoid overfitting pseudo-labels, several regularization losses are proposed to constrain the frequency information between target LR and SR images. Experiments show that without accessing source data, SOSR achieves superior results to the state-of-the-art UDA methods.

1. Introduction

Single image super-resolution (SISR), which is a fundamental task in low-level vision, aims to reconstruct a high-

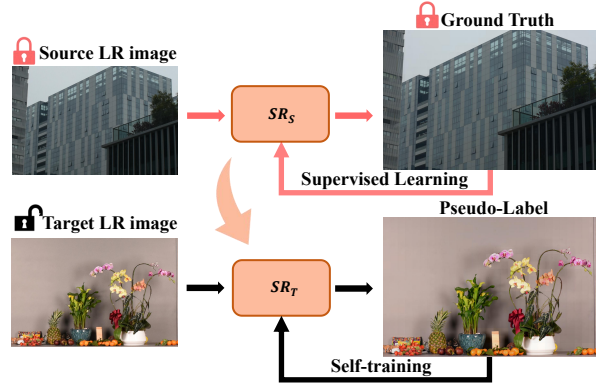


Figure 1: Overview of source-free image super-resolution. We can not access labeled source data during model adaptation.

resolution (HR) image from its low-resolution (LR) counterpart. In recent years, benefiting from the blossom of deep learning, a lot of deep learning based methods have been applied to single image super-resolution and achieved great success in this task. Most methods are based on CNN [5, 19] or Vision Transformer [6, 22].

However, a majority of existing methods are trained on synthetic datasets that synthesize the LR images via simple and determinate degradation kernel (e.g., bicubic), resulting in poor generalization towards real-world scenarios. To address this issue, a number of techniques have been proposed to explore the relationship between the HR and LR image pairs for real-world SISR, such as unsupervised learning [16, 29], domain adaptation [39, 42], and blind SISR [26]. In addition, some real-world datasets have been collected to train and evaluate real-world SISR methods, such as RealSR [4] and DRealSR [41]. These datasets include LR and HR image pairs captured on the same scene taken by different cameras. In the meanwhile, there exists a significant gap between degradation kernels for im-

ages captured by different cameras, which can be regarded as a cross-device domain gap. It is found that this kind of domain gap is harmful to the model’s performance in real-world scenarios [44].

To address this issue, Xu *et al.* [44] firstly propose an unsupervised domain adaptation (UDA) method for cross-device real-world image super-resolution. They design a dual framework with inter-domain and intra-domain adversarial adaptation to transfer the knowledge from the source domain to the target domain. This UDA method assumes the source data is accessible, which will be fed into the model to retain the source knowledge and relieve the domain shift. However, for many real-world applications, due to privacy policies or transmission restrictions, only the well-trained models are available while source data is absent. Unfortunately, existing UDA methods cannot be readily employed without the supervision of the source data.

As shown in Fig. 1, we propose in this paper and attempt to address a new and practical issue, namely Source-Free image Super-Resolution (SFSR). SFSR aims to adapt a model pre-trained on labeled source data to a target domain with only unlabeled target data. Recently, several Source Free Domain Adaptation (SFDA) methods [23, 24, 20, 27, 21] have been proposed to address similar challenges in image classification, semantic segmentation and object detection. These methods are designed specifically for classification tasks, aimed at obtaining reliable pseudo-labels or generating samples similar to the source domain distribution. However, when it comes to pixel-wise regression tasks such as image SR, these techniques are inapplicable.

In this paper, we present a novel method named SOSR, which is the first SOURCE-free image Super-Resolution framework. Due to the lack of supervision of the source data, we apply the strategy of pseudo-labeling for optimization of the target model. Inspired by [3, 32, 34, 43] adding noise (*e.g.*, data augmentation, dropout [33] and stochastic depth [13]) to the student model for better teacher-student learning in semi-supervised image classification, we firstly flip and rotate the target LR image to generate seven geometrically augmented images for pseudo-labels refinement. Furthermore, we propose a novel Wavelet Augmentation Transformer (WAT) to implicitly generate augmented data, which can be flexibly incorporated with existing networks. By performing a multi-level wavelet decomposition for latent features, WAT learns low-frequency information of varying levels across diverse samples. It performs a proposed Batch Augmentation Attention (BAA) at different levels to mix image features batch-wisely and efficiently fuse these features through deformable attention [52]. WAT enables the student model with the ability to learn and explore the appropriate augmentation in the feature space, which improves the robustness of the student model.

Beyond that, an uncertainty-aware self-training mecha-

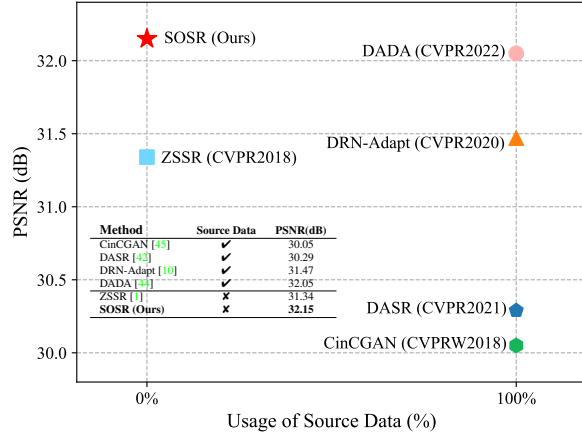


Figure 2: PSNR results vs. usage of source data for different methods on DRealSR [41] in the Olympus → Sony task. Our method performs favorably against existing state-of-the-art UDA and self-supervised methods.

nism is proposed to improve the accuracy of pseudo-labels by transferring knowledge from the target domain data to the teacher model. Specifically, the teacher network is updated with an exponential moving average of the student network to produce pseudo-labels. For one LR input, the teacher network runs multiple times to obtain the mean and variance as uncertainty estimation, which are then used to rectify pseudo-labels. Finally, in addition to the pixel-wise L1 loss and the perceptual loss using pseudo-labels, we introduce several regularization losses to constrain the frequency information between target LR and SR images. These loss functions effectively prevent the student network from overfitting pseudo-labels by mining frequency information in target LR images, which results in better SR results. The SOSR framework together with these losses successfully generalizes the pre-trained source model on the target domain. As shown in Fig. 2, SOSR achieves better PSNR against existing UDA and self-supervised methods without accessing source data.

The main contributions can be summarized as follows:

- We propose a novel SOSR framework to address the source-free image super-resolution (SFSR) problem. To the best of our knowledge, this is the first research on SFSR.
- We propose a novel wavelet augmentation transformer (WAT) to implicitly generate augmented data. WAT learns cross-level low-frequency information of varying levels across diverse samples effectively and improves the robustness of the student model.
- An uncertainty-aware self-training mechanism is introduced to improve the accuracy of pseudo-labels, with inaccurate predictions being rectified by uncertainty estimation. Several regularization losses are proposed

to avoid overfitting pseudo-labels.

- Extensive experiments show that our source-free SOSR outperforms state-of-the-art UDA methods.

2. Related Work

2.1. Single Image Super-Resolution

With the rapid and dramatic development of deep learning, more and more SISR models have been proposed and yielded state-of-the-art performance among diverse datasets. Dong *et al.* [5] present an approach to learning the mapping function from LR images to HR images just using three convolutional layers. After that, a mass of CNN-based architectures [36, 49, 25, 40, 11, 47, 48, 19, 17, 18] with more elaborate modules (*e.g.*, residual block, dense block, channel attention, non-local attention) have been proposed to improve the SISR performance. Recently, since the pioneering work Vision Transformer (ViT) [6] was proposed, the computer vision community has begun to explore the application of Transformer [37]. Compared with CNN-based methods, Transformer-based methods have great capability to capture global interactions. For SISR, Liang *et al.* [22] propose SwinIR and achieve state-of-the-art performance. However, due to the intractability to capture LR and HR image pairs, these methods are all trained on synthetic LR-HR image pairs, which results in the model’s poor generalization in real-world scenarios.

2.2. UDA for Real-World SISR

Nowadays, in order to circumvent the limitation resulted from the synthetic datasets, real-world SISR has attracted more and more attention in the community. Many approaches have been proposed to address this problem, such as unsupervised learning [16, 29, 45, 50], blind SISR [38, 9, 28, 2, 51]. Alternatively, Cai *et al.* [4] firstly build the RealSR dataset where LR-HR image pairs are captured on the same scene. Furthermore, DReasSR [41] has been constructed with images taken by five DSLR cameras. These cameras are equipped with different degradation kernels, which results in the cross-device domain gap between images captured by different cameras.

In fact, there are relatively few UDA methods available for real-world SISR. DASR [42] aims to address the domain gap between training data and testing data with domain-gap aware training and domain-distance weighted supervision strategies. Wang *et al.* [39] propose an SR training framework based on feature distribution alignment in a domain adaptation perspective. Xu *et al.* [44] firstly explore the cross-device real-world SR and proposed an unsupervised mechanism to address this cross-device domain gap. However, all these methods need to access the source data.

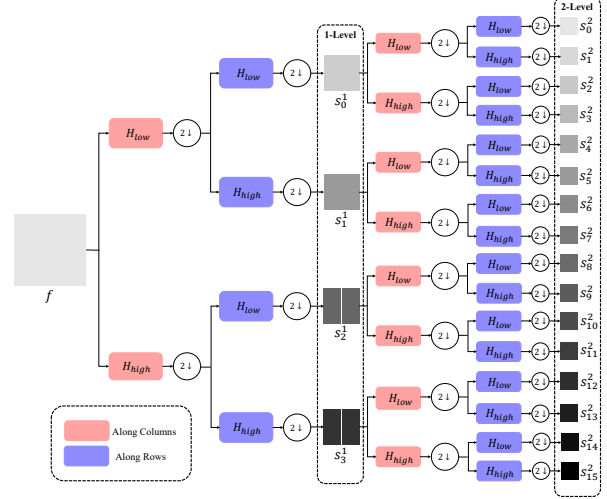


Figure 3: Illustration of 2-level haar wavelet packet transform (WPT). WPT employs low-pass filters H_{low} and high-pass filters H_{high} in a recursive manner to decompose the original features into multiple sub-bands at different frequency resolutions.

2.3. Source-Free Domain Adaptation

Recently, plenty of methods have been proposed to tackle SFDA for image classification, semantic segmentation and object detection. SHOT [23] and SHOT++ [24] freeze the classifier of the source model and match the output target features to source feature distribution with information maximization and pseudo-label strategy. 3C-GAN [20] generates labeled data with target domain style to improve the target model based on conditional GAN. SFDA [27] generates fake samples with a BNS constraint and designs a dual attention distillation mechanism to transfer and retain the contextual information for semantic segmentation. LODS [21] presents a style enhancement method to overlook target domain style in source-free object detection. However, all of these methods are specifically designed for classification tasks and cannot be directly applied to pixel-level regression tasks, such as SR. To our best knowledge, this paper is the first work for source-free SISR.

3. Methodology

3.1. Overview

According to the settings commonly used in the UDA task, the source dataset $D_s = \{(x_s^i, y_s^i)\}_{i=1}^{n_s}$ with n_s pairs of labeled samples and the target dataset $D_t = \{x_t^i\}_{i=1}^{n_t}$ with n_t unlabeled samples are given. In our source-free settings, the source dataset D_s is only accessible during pre-training. Our goal is to adapt the pre-trained source model to the target domain and get a better-performing target model without accessing the source data.

As shown in Fig. 4, SOSR is based on the teacher-student architecture. Both the teacher and student models consist of a head, a tail, and a feature extractor. After pre-training,

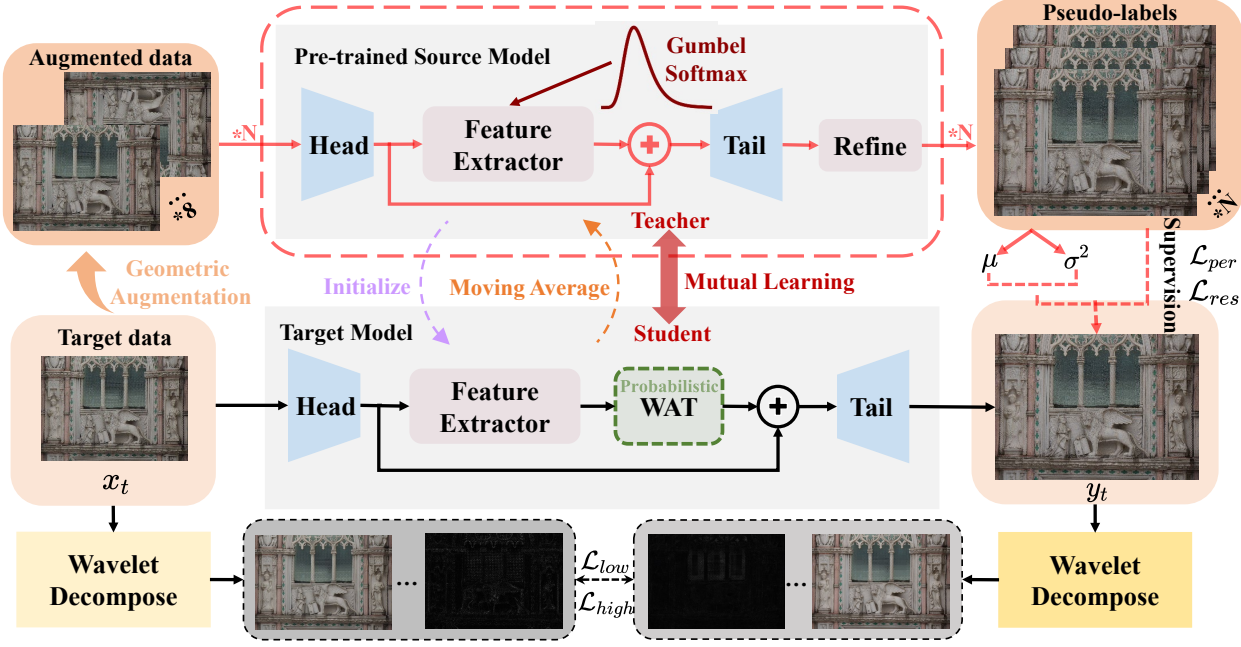


Figure 4: Architecture of the proposed SOSR framework. One target LR input together with its seven geometrically augmented images (*i.e.*, rotate and flip the input) will be fed into the teacher model to generate the refined pseudo-label. The Softmax normalization function in the teacher model will be replaced by Gumbel-Softmax [15]. For one LR input, the teacher model will run multiple times to generate N pseudo-labels and calculates their mean and variance for uncertainty estimation.

we can only access the well-trained teacher model f_ξ and unlabeled target data x_t , where ξ denotes the parameters of the teacher model. The student model f_θ has an additional wavelet augmentation transformer (WAT) module built upon the teacher model. Let θ_w denote the parameters of the WAT module and θ_o denote the parameters of other modules in the student model, excluding WAT. θ_o is initialized as the pre-trained teacher model. The proposed WAT is based on wavelet-transform, more specifically wavelet packet transform (WPT). As illustrated in Fig. 3, WPT can decompose the feature map into such sub-bands that have the same spatial size. Given a feature map of pixel-size $H \times W$ with a ℓ level WPT, we can get 4^ℓ sub-bands of pixel-size $\frac{H}{2^\ell} \times \frac{W}{2^\ell}$. WAT learns low-frequency information of varying levels using multi-level WPT.

SOSR consists of two distinct augmentation methods to facilitate teacher-student mutual learning. The first one is to rotate and flip one target LR image to generate seven geometrically augmented images. After feeding eight images into the teacher model to generate the SR images, the resulting SR images will be inverse transformed to their original geometry. The eight outputs will be averaged to produce the refined pseudo-label. Another is to use WAT to learn appropriate augmentation in the latent feature space. During training, there is a 50% probability that the feature maps extracted by the feature extractor will be fed into the WAT or not. Please note that WAT will not be utilized during

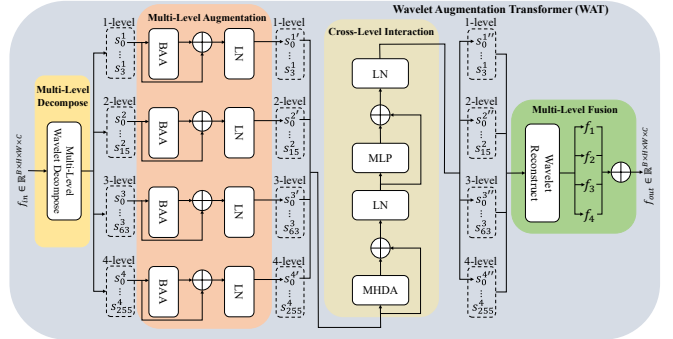


Figure 5: Wavelet Augmentation Transformer (WAT).

inference, resulting in no additional computational cost.

3.2. Wavelet Augmentation Transformer

As shown in Fig. 5, the WAT consists of four key modules: Multi-Level Decompose, Multi-Level Augmentation, Cross-Level Interaction, and Multi-Level Fusion.

Multi-Level Decompose. Given the input feature $f_{in} \in \mathbb{R}^{B \times H \times W \times C}$, WAT firstly employs a set of ℓ -level WPT to decompose it into multi-level wavelet sub-bands, *i.e.*, $\{s^{(\ell)} \in \mathbb{R}^{B \times m^{(\ell)} \times h^{(\ell)} \times w^{(\ell)} \times C} | \ell \in \mathcal{P}\}$, where $m^{(\ell)} = 4^\ell$, $h^{(\ell)} = \frac{H}{2^\ell}$, $w^{(\ell)} = \frac{W}{2^\ell}$ are the number, height, and width of the sub-bands, respectively; $\mathcal{P} = \{1, 2, 3, 4\}$ is a set of wavelet levels. Then we flatten them on the spatial dimension and get $\{s^{(\ell)} \in \mathbb{R}^{B \times m^{(\ell)} \times n^{(\ell)} \times C} | \ell \in \mathcal{P}\}$, where

$$n^{(\ell)} = h^{(\ell)} \times w^{(\ell)}.$$

Multi-level Augmentation. The proposed Batch Augmentation Attention (BAA) performs self-attention in a batch-wise manner. The latent features are mixed by the BAA batch-wisely to generate augmented data implicitly. To preserve the valuable high-frequency information in multi-level wavelet sub-bands, only the four low-frequency sub-bands, *i.e.*, $\{s_0^{(\ell)} | \ell \in P\}$, will be fed into BAA simultaneously. The four BAA modules do not share parameters.

Given $s_0^{(\ell)} \in \mathbb{R}^{B \times n^{(\ell)} \times C}$ as the input of the BAA. Firstly, we transpose the first two dimensions of $s_0^{(\ell)}$ so that $s_0^{(\ell)} \in \mathbb{R}^{n^{(\ell)} \times B \times C}$. Then it employs the standard self-attention mechanism for $s_0^{(\ell)}$; the query, key, and value matrices are calculated as

$$Q^{(\ell)} = s_0^{(\ell)} W_Q^{(\ell)}, K_i = s_0^{(\ell)} W_K^{(\ell)}, V_i = s_0^{(\ell)} W_V^{(\ell)}, \quad (1)$$

where $W_Q^{(\ell)}, W_K^{(\ell)}, W_V^{(\ell)} \in \mathbb{R}^{C \times C}$ are projection matrices. Then we have $Q^{(\ell)}, K^{(\ell)}, V^{(\ell)} \in \mathbb{R}^{n^{(\ell)} \times B \times C}$ and compute the output as

$$\text{SA}(s_0^{(\ell)}) = \text{softmax}\left(\frac{Q^{(\ell)}(K^{(\ell)})^T}{\sqrt{C}}\right)V^{(\ell)} \in \mathbb{R}^{n^{(\ell)} \times B \times C}, \quad (2)$$

where $(\cdot)^T$ represents the transpose of the second and third dimensions. Finally, we transpose the first two dimensions of the output. Then the final output of BAA has the same shape as the original $s_0^{(\ell)} \in \mathbb{R}^{B \times n^{(\ell)} \times C}$.

As shown in Fig. 5, the whole process of multi-level augmentation can be formulated as

$$s_0^{(\ell)'} = \text{LN}(\text{BAA}(s_0^{(\ell)}) + s_0^{(\ell)}). \quad (3)$$

Note that proposed multi-level augmentation module can learn low-frequency information of varying levels across diverse samples while also effectively preserving sensitive but valuable high-frequency information in image SR.

Cross-Level Interaction. Inspired from [52] that uses deformable attention to aggregate multi-scale feature maps in object detection, we employ the deformable attention to achieve cross-level information interaction.

As shown in Fig. 5, $\{s_0^{(\ell)'} | \ell \in P\}$ will be fed into the multi-head deformable attention (MHDA) module to facilitate information exchange across different levels, where $s_0^{(\ell)'} \in \mathbb{R}^{B \times n^{(\ell)} \times C}$. Firstly we concatenate them on the second dimension, denoted as $X' \in \mathbb{R}^{B \times N \times C}$, where $N = \sum_{\ell \in P} n^{(\ell)}$. Let $x' \in \mathbb{R}^{N \times C}$ denote one sample in X' . For the i^{th} feature $x'_i \in \mathbb{R}^C$ in x' , where $i \in \{1, \dots, N\}$, K features are sampled in each level for each attention head. Let $p_i \in [0, 1]^2$ be the normalized coordinates that represent the spatial position of x'_i in the original feature map. The position of sampling features can be denoted as

$p_{hlik} = p_i + \Delta p_{hlik}$, where Δp_{hlik} denotes the sampling offset of the k^{th} sampling point in the h^{th} attention head of the ℓ^{th} level. Bilinear interpolation is used to sample the feature and the sampled feature is denoted as x'_{hlik} for simplicity. The output of MHDA can be formulated as

$$x''_i = \sum_{h=1}^H W_h^{(1)} \left[\sum_{\ell \in P} \sum_{k=1}^K A_{hlik} W_h^{(2)} x'_{hlik} \right], \quad (4)$$

where H denotes the number of attention heads, $W_h^{(1)} \in \mathbb{R}^{C \times \frac{C}{H}}$ and $W_h^{(2)} \in \mathbb{R}^{\frac{C}{H} \times C}$ are projection matrices. A_{hlik} is the attention weight, which is obtained by projecting x'_i through a FC layer and normalizing it with softmax.

Through MHDA, the information across different levels can effectively interact. Then we employ a residual connection after the MHDA and MLP, respectively. The outputs of the residual connection are both fed into the LayerNorm layer:

$$\begin{aligned} X'' &= \text{LN}(\text{MHDA}(X') + X'), \\ X'' &= \text{LN}(\text{MLP}(X'') + X''), \end{aligned} \quad (5)$$

where $X'' \in \mathbb{R}^{B \times N \times C}$. Then we split it on the second dimension, we can recover the multi-level feature maps $\{s_0^{(\ell)''} | \ell \in P\}$, whose information has been effectively aggregated via MHDA across different levels.

Multi-Level Fusion. As shown in Fig. 5, we add up the four features after performing wavelet reconstruction on the wavelet sub-bands of different levels. Therefore, the output feature f_{out} combines information of different levels.

The proposed WAT performs BAA at different levels to mix image features batch-wisely and efficiently fuses these features through deformable attention. Note that WAT can be regarded as a novel form of model noise [43], which leverages the student model learn harder from the pseudo-labels and improves the robustness of the student model.

3.3. Uncertainty-aware Self-training Mechanism

When the domain gap between the source domain and the target domain is huge, the pseudo-labels generated from the teacher model may be unreliable. To further improve the accuracy of the pseudo-labels, we present an uncertainty-aware self-training mechanism to transfer the knowledge of unlabeled target data to the teacher model, with inaccurate predictions being rectified by uncertainty estimation.

Knowledge Transfer. As shown in Fig. 4, the parameters of the teacher network ξ are updated with an exponential moving average (EMA) of the parameters of the student network (excluding WAT) θ_o after each training step:

$$\xi = \eta \cdot \xi + (1 - \eta) \cdot \theta_o, \quad (6)$$

where $\eta \in [0, 1]$ is the decay rate, which is a hyper-parameter to control the update rate of the teacher network.

This approach has been proven effective in semi-supervised learning [34] and self-supervised learning [12, 8]. In our SOSR, the target domain knowledge learned by the student model can be slowly and progressively transferred to the teacher model via EMA, thereby improving the accuracy of pseudo-labels and promoting mutual learning between the teacher model and the student model.

Pseudo-label Rectification. Due to the domain gap between the source domain and the target domain, the pre-trained teacher model is inevitably prone to generating inaccurate pseudo-labels. In order to alleviate the adverse effects of inaccurate pseudo-labels, we incorporate uncertainty estimation into the self-training process to rectify the pseudo-labels.

Specifically, we replace the Softmax normalization function in the teacher model with Gumbel-Softmax [15] to introduce stochasticity in the generation of pseudo-labels. Given 1D vector $v \in \mathbb{R}^n$, the output of the Gumbel-Softmax is formulated as

$$v_i = \frac{\exp(\log(v_i + g_i)/\tau)}{\sum_{i=1}^n \exp((\log(v_i) + g_i)/\tau)}, \quad (7)$$

where g_i is sampled from a standard Gumbel distribution, and τ is a temperature parameter. g_i introduces stochasticity to the teacher model, enabling it to produce diverse SR results. As shown in Fig. 4, for one target LR input, we run the teacher model multiple times to generate N pseudo-labels y_p^1, \dots, y_p^N . Then we compute the mean and variance as the uncertainty estimation, which is formulated as

$$y_{mean} = \frac{1}{N} \sum_{n=1}^N y_p^n, \quad \sigma^2 = \frac{1}{N} \sum_{n=1}^N (y_p^n - y_{mean})^2. \quad (8)$$

Compared with existing methods, the proposed simple yet effective uncertainty estimation approach does not require additional components, *e.g.*, Batch Normalization [35] or Dropout [7], which may affect the SR results. Then we compute the pixel-level confidence map cof as following

$$cof = \beta - \text{Sigmoid}\left(\frac{\sigma^2}{\alpha}\right), \quad (9)$$

where α and β are hyper-parameters that adjust the value range of cof and they are set empirically to 0.0004 and 1.5, respectively. The confidence map reflects the magnitude of pixel-wise uncertainty. During training, we calculate the pixel-wise weighted L1 loss between the output of the student model f_θ and the averaged pseudo-labels y_{mean} using the confidence map:

$$\mathcal{L}_{rec} = \|cof \odot f_\theta(x_t) - cof \odot y_{mean}\|_1. \quad (10)$$

The inaccurate pseudo-labels will be rectified by the confidence map. The results in Sec. 4 show the effectiveness

of the proposed uncertainty-aware self-training in rectifying pseudo-labels. In addition to the L1 loss, we also calculate the perceptual loss between the two:

$$\mathcal{L}_{per} = \|\phi(f_\theta(x_t)) - \phi(y_{mean})\|_1, \quad (11)$$

where $\phi(\cdot)$ denotes the VGG-19 [30] feature extractor. Features from *conv5_3* layer are used to calculate the loss.

Regularization Losses. Furthermore, to prevent the student model from overfitting to pseudo-labels, two regularization losses are proposed to constrain the frequency information between LR and SR images. As shown in Fig. 4, we conduct wavelet decomposition on LR and SR images at different levels, ensuring that the resulting wavelet subbands have the same resolution. We impose L1 loss in the low-frequency space while adversarial loss in the high-frequency space. The L1 loss is defined as

$$\mathcal{L}_{low} = \left\| \text{wavelet}_{\mathcal{L}}^{(l1)}(x_t) - \text{wavelet}_{\mathcal{L}}^{(l2)}(f_\theta(x_t)) \right\|_1, \quad (12)$$

where $\text{wavelet}_{\mathcal{L}}^{(l*)}(\cdot)$ represents the low-frequency subband of l^* -level wavelet decomposition. The adversarial loss for the generator (*i.e.*, the student model) and the discriminator is respectively defined as

$$\mathcal{L}_{high}^G = -\mathbb{E}_{x_t} [\log(D(\text{wavelet}_{\mathcal{H}}^{(l2)}(f_\theta(x_t))))], \quad (13)$$

$$\begin{aligned} \mathcal{L}_{high}^D = & -\mathbb{E}_{x_t} [\log(D(\text{wavelet}_{\mathcal{H}}^{(l1)}(x_t)))] \\ & - \mathbb{E}_{x_t} [\log(1 - D(\text{wavelet}_{\mathcal{H}}^{(l2)}(f_\theta(x_t))))], \end{aligned} \quad (14)$$

where $\text{wavelet}_{\mathcal{H}}^{(l*)}(\cdot)$ represents the high-frequency subband of l^* -level wavelet decomposition.

Full objective function. The full objective function for the student model f_θ is defined as

$$\mathcal{L} = \mathcal{L}_{rec} + \lambda_1 \mathcal{L}_{per} + \lambda_2 \mathcal{L}_{low} + \lambda_3 \mathcal{L}_{high}^G, \quad (15)$$

where $\lambda_{1\sim 3}$ are hyper-parameters to balance each item.

4. Experiments

4.1. Datasets and Metrics

We evaluate our method on the DRealSR [41] dataset. DRealSR is a large-scale real-world SR benchmark, which is collected by five DSLR cameras (*i.e.*, Panasonic, Sony, Olympus, Nikon, and Canon) in real-world scenarios. Following [44], we choose images captured from three cameras (Panasonic, Sony, and Olympus) for our experiments, which contain 197, 145, and 190 image pairs for training; 20, 17, and 19 image pairs for testing, respectively. The image SR performance is evaluated by calculating PSNR, SSIM, and LPIPS [46]. PSNR and SSIM are computed on the Y channel and the RGB space, respectively.

Method	SF	Panasonic \rightarrow Sony			Sony \rightarrow Panasonic			Olympus \rightarrow Panasonic		
		PSNR \uparrow	SSIM \uparrow	LPIPS \downarrow	PSNR \uparrow	SSIM \uparrow	LPIPS \downarrow	PSNR \uparrow	SSIM \uparrow	LPIPS \downarrow
Real \rightarrow Real										
Target Only	\times	32.45	0.854	0.298	32.13	0.841	0.312	32.13	0.841	0.312
Source Only	\times	31.44	0.841	0.302	30.82	0.820	0.371	30.54	0.818	0.372
CinCGAN [45]	\times	27.76	0.821	0.391	28.33	0.792	0.410	29.37	0.799	0.381
DASR [42]	\times	30.08	0.777	0.269	30.45	0.772	0.316	30.06	0.785	0.272
DRN-Adapt [10]	\times	31.85	0.845	0.321	30.96	0.821	0.380	30.80	0.822	0.356
DADA [44]	\times	32.13	0.849	0.327	31.25	0.825	0.363	31.27	0.824	0.348
SOSR (Ours)	\checkmark	32.22	0.851	0.296	31.32	0.826	0.330	31.34	0.826	0.330
Synthetic \rightarrow Real										
Source Only	\times	31.44	0.826	0.346	30.46	0.806	0.417	30.49	0.806	0.414
CinCGAN [45]	\times	27.59	0.788	0.405	27.19	0.743	0.414	28.38	0.739	0.422
DASR [42]	\times	29.95	0.764	0.298	29.79	0.749	0.339	30.02	0.777	0.293
DRN-Adapt [10]	\times	31.42	0.829	0.359	30.47	0.808	0.429	30.45	0.808	0.433
DADA [44]	\times	31.50	0.830	0.369	30.72	0.809	0.376	30.74	0.808	0.362
SOSR(Ours)	\checkmark	31.58	0.831	0.355	30.77	0.810	0.374	30.78	0.809	0.360
Method	SF	Panasonic \rightarrow Olympus			Sony \rightarrow Olympus			Olympus \rightarrow Sony		
		PSNR \uparrow	SSIM \uparrow	LPIPS \downarrow	PSNR \uparrow	SSIM \uparrow	LPIPS \downarrow	PSNR \uparrow	SSIM \uparrow	LPIPS \downarrow
Real \rightarrow Real										
Target Only	\times	31.35	0.827	0.381	31.35	0.827	0.381	32.45	0.854	0.298
Source Only	\times	30.33	0.816	0.424	30.60	0.808	0.452	30.35	0.813	0.308
CinCGAN [45]	\times	28.85	0.791	0.461	30.17	0.814	0.443	30.05	0.823	0.365
DASR [42]	\times	29.32	0.768	0.306	29.86	0.762	0.372	30.29	0.787	0.270
DRN-Adapt [10]	\times	30.73	0.816	0.431	30.66	0.810	0.459	31.47	0.833	0.312
DADA [44]	\times	31.08	0.820	0.433	31.08	0.817	0.438	32.05	0.843	0.343
SOSR (Ours)	\checkmark	31.15	0.821	0.391	31.17	0.820	0.394	32.15	0.845	0.281
Synthetic \rightarrow Real										
Source Only	\times	30.15	0.796	0.454	30.14	0.796	0.456	31.45	0.828	0.344
CinCGAN [45]	\times	28.43	0.766	0.407	29.34	0.767	0.451	29.50	0.792	0.392
DASR [42]	\times	28.30	0.752	0.375	29.51	0.755	0.402	29.40	0.737	0.327
DRN-Adapt [10]	\times	30.11	0.799	0.475	30.11	0.799	0.473	31.45	0.829	0.362
DADA [44]	\times	30.40	0.800	0.403	30.62	0.803	0.411	31.52	0.829	0.355
SOSR(Ours)	\checkmark	30.43	0.801	0.421	30.66	0.804	0.400	31.57	0.830	0.342

Table 1: Quantitative comparison with state-of-the-art UDA methods for $\times 4$ SR. "SF" represents whether the method is under source-free setting. Except *Target Only*, the best and second best performance are in red and blue colors, respectively.

Panasonic Testset				Sony Testset				Olympus Testset			
Method	PSNR \uparrow	SSIM \uparrow	LPIPS \downarrow	Method	PSNR \uparrow	SSIM \uparrow	LPIPS \downarrow	Method	PSNR \uparrow	SSIM \uparrow	LPIPS \downarrow
MZSR [31]	28.73	0.785	0.398	MZSR [31]	29.00	0.796	0.366	MZSR [31]	28.54	0.777	0.443
ZSSR [1]	30.42	0.805	0.417	ZSSR [1]	31.34	0.823	0.344	ZSSR [1]	30.06	0.794	0.455
Ours (S \rightarrow P)	31.32	0.826	0.330	Ours (O \rightarrow S)	32.15	0.845	0.281	Ours (P \rightarrow O)	31.15	0.821	0.391
Ours (O \rightarrow P)	31.34	0.826	0.330	Ours (P \rightarrow S)	32.22	0.851	0.296	Ours (S \rightarrow O)	31.17	0.820	0.394

Table 2: Quantitative comparison with some typical self-supervised SR methods for $\times 4$ SR. "P", "S" and "O" represent Panasonic, Sony and Olympus, respectively. Best and second best performance are in red and blue colors, respectively. For the test set of one camera, our method has two adaptation settings.

4.2. Implementation Details

The classical SwinIR [22] network is employed as the backbone for image SR. The discriminator we adopted is PatchGAN [14]. We use the Adam optimizer with $\beta_1 = 0.9$, $\beta_2 = 0.999$ and a fixed learning rate of 2×10^{-6} . In each iteration, the proposed framework is trained on the image patches of size 48×48 with a batch-size of 32. During training, we adopt the data augmentation methods of random crop, flip, and rotation. The decay rate η in Eq. (6) is set to 0.999 to make the training process more stable. The temperature parameter τ in Eq. (7) is set to 0.1 to mitigate the impact on the performance of the teacher model

while introducing uncertainty estimation. The N in Eq. (8) is set to 5 to calculate the mean and variance. The levels of wavelet decomposition l_1 and l_2 in Eq. (12) are set to 1 and 3, respectively. For hyper-parameters in Eq. (15), the loss weights $\lambda_1, \lambda_2, \lambda_3$ are set to 0.01, 0.1, and 0.005, respectively. The proposed framework will converge after about 4000 iterations. The student model without WAT is used for inference, leading to no additional computational cost.

4.3. Comparison with state-of-the-art methods

Due to the absence of the source-free method for real-world image SR, we compare our SOSR with the state-of-the-art UDA methods and some typical self-supervised

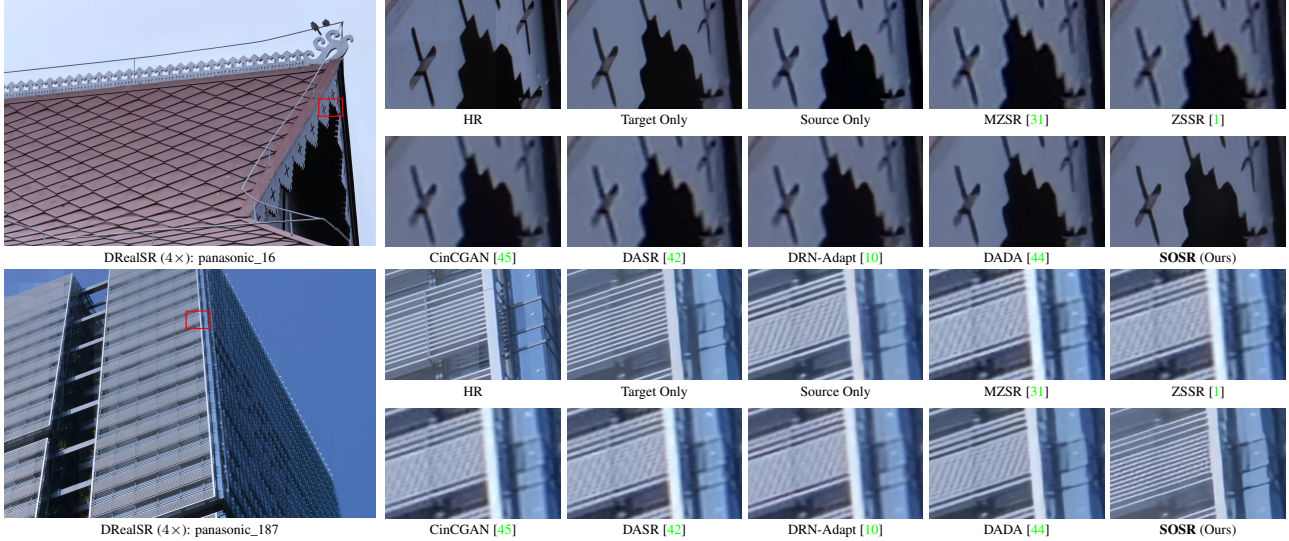


Figure 6: Visual comparison for $\times 4$ SR on DRealSR dataset (Sony \rightarrow Panasonic). Best viewed with zoom in.

methods for real-world image SR. The competing UDA methods include CinCGAN [45], DASR [42], DRN-Adapt [10] and DADA [44] while self-supervised methods include ZSSR [1] and MZSR [31]. Our experiments include real \rightarrow real adaptation and synthetic \rightarrow real adaptation. In real \rightarrow real adaptation task, our source model is trained on the real-world image pairs from the DRealSR. In contrast to this, in synthetic \rightarrow real adaptation task, our source model is trained on synthetic image pairs (*i.e.*, LR images are bicubically downsampled from the real-world HR images). Our experiments are for scaling factor $\times 4$.

Table 1 shows the quantitative results in six camera \rightarrow camera adaptation tasks. "Source only" represents the model trained on the source data without domain adaptation. "Target only" represents the model trained on the target labeled data. In six real \rightarrow real tasks, our method achieves the best performance on the PSNR and SSIM metrics and the second best performance on the LPIPS metric without accessing the source data. Although DASR achieves the best LPIPS, its PSNR and SSIM are inferior to ours, and it often produces SR images containing artifacts and noises. In six synthetic \rightarrow real tasks, our method also performs better than other methods. Table 2 shows the quantitative results compared with self-supervised SR methods on three test set. ZSSR and MZSR require only a single LR image to train a SR network specifically tailored to that LR image. Since our method preserves the domain-invariant knowledge in the pre-trained source model and reduces the cross-domain discrepancy by model adaptation, our method performs much better than the self-supervised SR methods.

Fig. 6 shows that our method can not only reason the correct structure of the buildings, but also generate clear details, while other methods may generate deformed structure



Figure 7: Visual illustration of the uncertainty estimation.

Metrics	Source Only	w/o WAT	w/o EMA	w/o Reg. Loss	w/o UE	Ours
PSNR \uparrow	31.44	31.60	31.92	32.15	32.16	32.22
SSIM \uparrow	0.841	0.843	0.844	0.849	0.849	0.851
LPIPS \downarrow	0.302	0.306	0.304	0.304	0.298	0.296

Table 3: Ablation results on DRealSR.

and blurry results. The results of our method are closest to those trained with target labels.

4.4. Ablation Study

We conduct an ablation study in the Panasonic \rightarrow Sony task to evaluate the respective roles of each part of our method. As shown in Table 3, the performance drops a lot when separately removing WAT and EMA. This demonstrates the significant role of WAT and EMA in facilitating the teacher-student learning. The results also demonstrate that the regularization loss and uncertainty estimation (UE) can improve the quality of SR images. As shown in Fig. 7, pixels with higher error in the pseudo-label will be assigned lower confidence, which also proves the effectiveness of the proposed uncertainty estimation method. Due to space limitations, a detailed analysis of these components and hyper-parameters in our method is provided in the Appendix.

5. Conclusion

In this paper, we propose a novel framework SOSR for real-world source-free image super-resolution. It attempts

to adapt the source model to the target domain without accessing source data. By using our proposed wavelet augmentation transformer (WAT), the student model is capable of learning low-frequency information of varying levels across diverse samples, which is aggregated efficiently via deformable attention. Besides, an uncertainty-aware self-training mechanism is proposed to facilitate knowledge transfer and rectify pseudo-labels. Several regularization losses are proposed to avoid overfitting pseudo-labels. Extensive experiments under the six adaptation settings of real \rightarrow real and synthetic \rightarrow real on DRealSR dataset demonstrate the effectiveness of our method. Theoretically, our approach is not limited to image super-resolution but rather can be extended to other real-world low-level vision tasks.

References

- [1] Michal Irani Assaf Shocher, Nadav Cohen. "zero-shot" super-resolution using deep internal learning. In *CVPR*, pages 3118–3126, 2018. [2](#), [7](#), [8](#), [15](#)
- [2] Sefi Bell-Kligler, Assaf Shocher, and Michal Irani. Blind super-resolution kernel estimation using an internal-gan. In *NeurIPS*, pages 284–293, 2019. [3](#)
- [3] David Berthelot, Nicholas Carlini, Ian Goodfellow, Nicolas Papernot, Avital Oliver, and Colin A Raffel. Mixmatch: A holistic approach to semi-supervised learning. In *NeurIPS*, pages 5049–5059, 2019. [2](#)
- [4] Jianrui Cai, Hui Zeng, Hongwei Yong, Zisheng Cao, and Lei Zhang. Toward real-world single image super-resolution: A new benchmark and a new model. In *ICCV*, pages 3086–3095, 2019. [1](#), [3](#)
- [5] Chao Dong, Chen Change Loy, Kaiming He, and Xiaoou Tang. Image super-resolution using deep convolutional networks. *TPAMI*, 38(2):295–307, 2015. [1](#), [3](#)
- [6] Alexey Dosovitskiy, Lucas Beyer, Alexander Kolesnikov, Dirk Weissenborn, Xiaohua Zhai, Thomas Unterthiner, Mostafa Dehghani, Matthias Minderer, Georg Heigold, Sylvain Gelly, et al. An image is worth 16x16 words: Transformers for image recognition at scale. In *ICLR*, 2021. [1](#), [3](#)
- [7] Yarin Gal and Zoubin Ghahramani. Dropout as a bayesian approximation: Representing model uncertainty in deep learning. In *ICML*, pages 1050–1059, 2016. [6](#)
- [8] Jean-Bastien Grill, Florian Strub, Florent Altché, Corentin Tallec, Pierre Richemond, Elena Buchatskaya, Carl Doersch, Bernardo Avila Pires, Zhaohan Guo, Mohammad Gheshlaghi Azar, et al. Bootstrap your own latent—a new approach to self-supervised learning. In *NeurIPS*, pages 21271–21284, 2020. [6](#)
- [9] Jinjin Gu, Hannan Lu, Wangmeng Zuo, and Chao Dong. Blind super-resolution with iterative kernel correction. In *CVPR*, pages 1604–1613, 2019. [3](#)
- [10] Yong Guo, Jian Chen, Jingdong Wang, Qi Chen, Jiezhong Cao, Zeshuai Deng, Yanwu Xu, and Minghui Tan. Closed-loop matters: Dual regression networks for single image super-resolution. In *CVPR*, pages 5407–5416, 2020. [2](#), [7](#), [8](#), [15](#)
- [11] Muhammad Haris, Gregory Shakhnarovich, and Norimichi Ukita. Deep back-projection networks for super-resolution. In *CVPR*, pages 1664–1673, 2018. [3](#)
- [12] Kaiming He, Haoqi Fan, Yuxin Wu, Saining Xie, and Ross Girshick. Momentum contrast for unsupervised visual representation learning. In *CVPR*, pages 9729–9738, 2020. [6](#)
- [13] Gao Huang, Yu Sun, Zhuang Liu, Daniel Sedra, and Kilian Q Weinberger. Deep networks with stochastic depth. In *ECCV*, pages 646–661, 2016. [2](#)
- [14] Phillip Isola, Jun-Yan Zhu, Tinghui Zhou, and Alexei A Efros. Image-to-image translation with conditional adversarial networks. In *CVPR*, pages 1125–1134, 2017. [7](#), [11](#)
- [15] Eric Jang, Shixiang Gu, and Ben Poole. Categorical reparameterization with gumbel-softmax. In *ICLR*, 2017. [4](#), [6](#), [12](#)
- [16] Gwan-tae Kim, Jaihyun Park, Kanghyu Lee, Junyeop Lee, Jeongki Min, Bokyeung Lee, David K Han, and Hanseok Ko. Unsupervised real-world super resolution with cycle generative adversarial network and domain discriminator. In *CVPR*, pages 456–457, 2020. [1](#), [3](#)
- [17] Jiwon Kim, Jung Kwon Lee, and Kyoung Mu Lee. Accurate image super-resolution using very deep convolutional networks. In *CVPR*, pages 1646–1654, 2016. [3](#)
- [18] Wei-Sheng Lai, Jia-Bin Huang, Narendra Ahuja, and Ming-Hsuan Yang. Fast and accurate image super-resolution with deep laplacian pyramid networks. *TPAMI*, 41(11):2599–2613, 2018. [3](#)
- [19] Christian Ledig, Lucas Theis, Ferenc Huszár, Jose Caballero, Andrew Cunningham, Alejandro Acosta, Andrew Aitken, Alykhan Tejani, Johannes Totz, Zehan Wang, et al. Photo-realistic single image super-resolution using a generative adversarial network. In *CVPR*, pages 4681–4690, 2017. [1](#), [3](#)
- [20] Rui Li, Qianfen Jiao, Wenming Cao, Hau-San Wong, and Si Wu. Model adaptation: Unsupervised domain adaptation without source data. In *CVPR*, pages 9641–9650, 2020. [2](#), [3](#)
- [21] Shuaifeng Li, Mao Ye, Xiatian Zhu, Lihua Zhou, and Lin Xiong. Source-free object detection by learning to overlook domain style. In *CVPR*, pages 8014–8023, 2022. [2](#), [3](#), [11](#)
- [22] Jingyun Liang, Jiezhong Cao, Guolei Sun, Kai Zhang, Luc Van Gool, and Radu Timofte. Swinir: Image restoration using swin transformer. In *ICCV Workshops*, pages 1833–1844, 2021. [1](#), [3](#), [7](#), [11](#)
- [23] Jian Liang, Dapeng Hu, and Jiashi Feng. Do we really need to access the source data? source hypothesis transfer for unsupervised domain adaptation. In *ICML*, pages 6028–6039, 2020. [2](#), [3](#), [11](#)
- [24] Jian Liang, Dapeng Hu, Yunbo Wang, Ran He, and Jiashi Feng. Source data-absent unsupervised domain adaptation through hypothesis transfer and labeling transfer. *TPAMI*, 44(11):8602–8617, 2022. [2](#), [3](#), [11](#)
- [25] Bee Lim, Sanghyun Son, Heewon Kim, Seungjun Nah, and Kyoung Mu Lee. Enhanced deep residual networks for single image super-resolution. In *CVPR Workshops*, pages 136–144, 2017. [3](#)
- [26] Anran Liu, Yihao Liu, Jinjin Gu, Yu Qiao, and Chao Dong. Blind image super-resolution: A survey and beyond. *arXiv preprint arXiv:2107.03055*, 2021. [1](#)

- [27] Yuang Liu, Wei Zhang, and Jun Wang. Source-free domain adaptation for semantic segmentation. In *CVPR*, pages 1215–1224, 2021. [2](#), [3](#), [11](#)
- [28] Zhengxiong Luo, Yan Huang, Shang Li, Liang Wang, and Tieniu Tan. Unfolding the alternating optimization for blind super resolution. In *NeurIPS*, pages 5632–5643, 2020. [3](#)
- [29] Kalpesh Prajapati, Vishal Chudasama, Heena Patel, Kishor Upla, Raghavendra Ramachandra, Kiran Raja, and Christoph Busch. Unsupervised single image super-resolution network (usisresnet) for real-world data using generative adversarial network. In *CVPR Workshops*, pages 464–465, 2020. [1](#), [3](#)
- [30] K. Simonyan and Andrew Zisserman. Very deep convolutional networks for large-scale image recognition. *arXiv preprint arXiv:1409.1556*, 2014. [6](#)
- [31] Jae Woong Soh, Sunwoo Cho, and Nam Ik Cho. Meta-transfer learning for zero-shot super-resolution. In *CVPR*, pages 3516–3525, 2020. [7](#), [8](#), [15](#)
- [32] Kihyuk Sohn, David Berthelot, Nicholas Carlini, Zizhao Zhang, Han Zhang, Colin A Raffel, Ekin Dogus Cubuk, Alexey Kurakin, and Chun-Liang Li. Fixmatch: Simplifying semi-supervised learning with consistency and confidence. In *NeurIPS*, pages 596–608, 2020. [2](#)
- [33] Nitish Srivastava, Geoffrey Hinton, Alex Krizhevsky, Ilya Sutskever, and Ruslan Salakhutdinov. Dropout: a simple way to prevent neural networks from overfitting. *JMLR*, 15(1):1929–1958, 2014. [2](#)
- [34] Antti Tarvainen and Harri Valpola. Mean teachers are better role models: Weight-averaged consistency targets improve semi-supervised deep learning results. In *NeurIPS*, pages 1195–1204, 2017. [2](#), [6](#)
- [35] Mattias Teye, Hossein Azizpour, and Kevin Smith. Bayesian uncertainty estimation for batch normalized deep networks. In *ICML*, pages 4907–4916, 2018. [6](#)
- [36] Chunwei Tian, Yanning Zhang, Wangmeng Zuo, Chiao Wen Lin, David Zhang, and Yixuan Yuan. A heterogeneous group cnn for image super-resolution. *arXiv preprint arXiv:2209.12406*, 2022. [3](#)
- [37] Ashish Vaswani, Noam Shazeer, Niki Parmar, Jakob Uszkoreit, Llion Jones, Aidan N Gomez, Łukasz Kaiser, and Illia Polosukhin. Attention is all you need. In *NeurIPS*, pages 5998–6008, 2017. [3](#)
- [38] Longguang Wang, Yingqian Wang, Xiaoyu Dong, Qingyu Xu, Jungang Yang, Wei An, and Yulan Guo. Unsupervised degradation representation learning for blind super-resolution. In *CVPR*, pages 10581–10590, 2021. [3](#)
- [39] Wei Wang, Haochen Zhang, Zehuan Yuan, and Changhu Wang. Unsupervised real-world super-resolution: A domain adaptation perspective. In *ICCV*, pages 4318–4327, 2021. [1](#), [3](#)
- [40] Xintao Wang, Ke Yu, Shixiang Wu, Jinjin Gu, Yihao Liu, Chao Dong, Chen Change Loy, Yu Qiao, and Xiaoou Tang. Esrgan: Enhanced super-resolution generative adversarial networks. *arXiv preprint arXiv:1809.00219*, 2018. [3](#)
- [41] Pengxu Wei, Ziwei Xie, Hannan Lu, Zongyuan Zhan, Qixiang Ye, Wangmeng Zuo, and Liang Lin. Component divide-and-conquer for real-world image super-resolution. In *ECCV*, pages 101–117, 2020. [1](#), [2](#), [3](#), [6](#), [13](#)
- [42] Yunxuan Wei, Shuhang Gu, Yawei Li, Radu Timofte, Longcun Jin, and Hengjie Song. Unsupervised real-world image super resolution via domain-distance aware training. In *CVPR*, pages 13385–13394, 2021. [1](#), [2](#), [3](#), [7](#), [8](#), [15](#)
- [43] Qizhe Xie, Minh-Thang Luong, Eduard Hovy, and Quoc V Le. Self-training with noisy student improves imagenet classification. In *CVPR*, pages 10687–10698, 2020. [2](#), [5](#), [11](#)
- [44] Xiaoqian Xu, Pengxu Wei, Weikai Chen, Yang Liu, Mingzhi Mao, Liang Lin, and Guanbin Li. Dual adversarial adaptation for cross-device real-world image super-resolution. In *CVPR*, pages 5667–5676, 2022. [2](#), [3](#), [6](#), [7](#), [8](#), [15](#)
- [45] Yuan Yuan, Siyuan Liu, Jiawei Zhang, Yongbing Zhang, Chao Dong, and Liang Lin. Unsupervised image super-resolution using cycle-in-cycle generative adversarial networks. In *CVPR Workshops*, pages 701–710, 2018. [2](#), [3](#), [7](#), [8](#), [15](#)
- [46] Richard Zhang, Phillip Isola, Alexei A. Efros, Eli Shechtman, and Oliver Wang. The unreasonable effectiveness of deep features as a perceptual metric. In *CVPR*, pages 586–595, 2018. [6](#)
- [47] Yulun Zhang, Kunpeng Li, Kai Li, Lichen Wang, Bineng Zhong, and Yun Fu. Image super-resolution using very deep residual channel attention networks. In *ECCV*, pages 286–301, 2018. [3](#)
- [48] Yulun Zhang, Yapeng Tian, Yu Kong, Bineng Zhong, and Yun Fu. Residual dense network for image super-resolution. In *CVPR*, pages 2472–2481, 2018. [3](#)
- [49] Yulun Zhang, Yapeng Tian, Yu Kong, Bineng Zhong, and Yun Fu. Residual dense network for image restoration. *TPAMI*, 43(7):2480–2495, 2021. [3](#)
- [50] Tianyu Zhao, Wenqi Ren, Changqing Zhang, Dongwei Ren, and Qinghua Hu. Unsupervised degradation learning for single image super-resolution. *arXiv preprint arXiv:1812.04240*, 2018. [3](#)
- [51] Ruofan Zhou and Sabine Susstrunk. Kernel modeling super-resolution on real low-resolution images. In *ICCV*, pages 2433–2443, 2019. [3](#)
- [52] Xizhou Zhu, Weijie Su, Lewei Lu, Bin Li, Xiaogang Wang, and Jifeng Dai. Deformable detr: Deformable transformers for end-to-end object detection. In *ICLR*, 2021. [2](#), [5](#)

A. Appendix

A.1. Differences between SFSR and other tasks

Recently, several SFDA methods have been proposed to tackle similar challenges in classification tasks (*e.g.*, image classification, semantic segmentation, and object detection). For image classification, SHOT [23] and SHOT++ [24] adopt the pseudo-labeling strategy and iteratively update the pseudo-labels using the centroid of each class. For semantic segmentation, [27] generates fake samples with a BNS constraint, which is only applicable to backbones that contain Batch Normalization layers. It divides each sample into patches and splits them into easy and hard groups by entropy-ranking for model adaptation. For object detection, LODS [21] presents a style enhancement method and utilizes graph based class-wise instance-level alignment to overlook the target domain style.

Although these techniques can be extended to other analogous classification tasks, they cannot be directly applied to pixel-level regression tasks. Pixel-level regression tasks, such as SR, do not involve the notion of classes. Consequently, it is not feasible to utilize distinct classes to rectify pseudo-labels or achieve feature alignment. Hence, it is of great importance to tackle source-free image super-resolution (SFSR) by taking into account the unique attributes of the SR task.

A.2. Training Algorithm

The training process of the proposed SOSR includes two stages. Firstly, we pre-train the source model on the labeled source dataset using supervised learning and obtain a well-trained source model f_ξ . After that, we adapt the pre-trained model towards the target domain without accessing source data using Algorithm 1.

A.3. Network Architecture

The classical SwinIR [22] network is employed as the backbone for our SOSR. For the discriminator in this paper, we adopt PatchGAN [14] used in SwinIR. For the multi-head deformable attention module, the number of sampled features K and attention heads H in Eq. (4) are set to 4 and 6, respectively.

A.4. Ablation Study

As mentioned in the main text of the paper, we conduct a detailed analysis of each component in our method in this section. For the sake of readability, we provide the result of the ablation study again in Table. 4. Besides, we conduct an analysis for hyper-parameters η and λ_{1-3} in Eq. (6) and Eq. (15). Due to the proposed BAA in WAT being related to batch size, we also analyze the effect of batch size on results in Table. 9.

Algorithm 1 Model adaptation on unlabeled target data

```

1:  $\xi \leftarrow$  Pre-trained weights of the teacher model  $f_\xi$ 
2:  $\theta_w \leftarrow$  Randomly initialize WAT in the student model
3:  $\theta_o \leftarrow \xi$   $\triangleright$  Perform deepcopy for other modules in the
   student model (excluding WAT)
4:  $\theta \leftarrow$  Weights of the student model  $f_\theta$ 
5:  $\varphi \leftarrow$  Randomly initialize discriminator  $D$ 
6: while not converged do
7:    $X_T \leftarrow$  Random batch from unlabeled target dataset
8:    $\{X_{TA^{(i)}} \mid i = 1, \dots, 8\} \leftarrow Aug(X_T)$   $\triangleright$  Perform
   geometric augmentation for  $X_T$ 
9:   for  $n=1:N$  do  $\triangleright$  Produce multiple predictions
10:     $Y_{PA^{(i)}}^{(n)} \leftarrow f_\xi(X_{TA^{(i)}})$   $\triangleright$  Produce pseudo-labels
11:     $Y_P^{(n)} \leftarrow Refine(Y_{PA^{(i)}}^{(n)})$   $\triangleright$  Produce refined
   pseudo-labels
12:   end for
13:    $Y_{Mean} \leftarrow \frac{1}{N} \sum_{n=1}^N Y_P^{(n)}$ 
14:    $\sigma^2 \leftarrow \frac{1}{N} \sum_{n=1}^N (Y_P^{(n)} - Y_{Mean})^2$ 
15:    $cof \leftarrow \beta - \text{Sigmoid}(\frac{\sigma^2}{\alpha})$   $\triangleright$  Confidence Map
16:    $Y_T \leftarrow f_\theta(X_T)$ 
17:    $L^D \leftarrow L_{high}^D(D(X_T), D(Y_T))$ 
18:    $\varphi \leftarrow \varphi - \lambda \nabla_\varphi L^D$   $\triangleright$  Perform Adam updates for  $\varphi$ 
19:    $L \leftarrow L_{rec}(Y_T, Y_{Mean}) + \lambda_1 L_{per}(Y_T, Y_{Mean}) +$ 
    $\lambda_2 L_{low}(X_T, Y_T) + \lambda_3 L_{high}^G(D(Y_T))$ 
20:    $\theta \leftarrow \theta - \lambda \nabla_\theta L$   $\triangleright$  Perform Adam updates for  $\theta$ 
21:    $\xi \leftarrow \eta \cdot \xi + (1 - \eta) \cdot \theta_o$   $\triangleright$  Perform EMA for  $\xi$ 
22: end while

```

Metrics	Source Only	w/o WAT	w/o EMA	w/o Reg. Loss	w/o UE	Ours
PSNR \uparrow	31.44	31.60	31.92	32.15	32.16	32.22
SSIM \uparrow	0.841	0.843	0.844	0.849	0.849	0.851
LPIPS \downarrow	0.302	0.306	0.304	0.304	0.298	0.296

Table 4: Ablation results on DRealSR.

WAT. The proposed WAT enables the student model with the ability to learn and explore the appropriate augmentation in the latent feature space, which improves the robustness of the student model. It can be regarded as a novel form of model noise [43] to make the student model learn harder from the pseudo-labels. Besides, WAT preserves the valuable high-frequency information in multi-level wavelet sub-bands, which contributes to better SR results. As shown in Table. 4, the performance decreases a lot when removing WAT from SOSR. It demonstrates that WAT is important for facilitating teacher-student mutual learning. The proposed BAA in WAT is related to batch size. Table. 9 shows that when the batch size is changed from 16 to 128, the performance of the method does not change significantly. It proves that WAT is insensitive to the batch size.

EMA. The proposed EMA aims to progressively transfer

the target domain knowledge learned by the student model to the teacher model. Table. 4 shows that removing EMA will lead to a decrease in performance. It proves that EMA contributes to improving the accuracy of pseudo-labels and promoting mutual learning between the teacher model and the student model. We also analyze the impact of different decay rate η on the experimental results in Table. 5. The decay rate η in Eq. (6) governs the updating speed of the teacher model. When $\eta = 0$, the teacher model is updated to be the same as the student model (excluding WAT). When $\eta = 1$, the teacher model will not be updated. When the update rate is too fast (e.g., $\eta = 0$), the training process becomes unstable, leading to a significant decrease in performance. When the update rate is very slow (e.g., $\eta = 0.9999$), the performance improvement is relatively small. Therefore, we set η to 0.999 as a trade-off.

Regularization Losses. The regularization losses are proposed to constrain the frequency information between target LR and SR images. Removing it will result in a slight performance degradation. It is helpful to prevent the student model from overfitting to pseudo-labels. Results of different loss weights λ_2 and λ_3 on DRealSR are provided in Table. 7 and Table. 8, respectively. Note that large λ_3 may lead to training instability and performance drop.

UE. The uncertainty estimation is helpful to rectify the inaccurate pseudo-labels. The confidence map assigns varying weights based on the uncertainty of each pixel in the pseudo-labels for optimizing the student network. Removing it from our approach would result in a minor performance degradation. More insights about UE will be introduced in Sec. A.5.

η	PSNR \uparrow	SSIM \uparrow	LPIPS \downarrow
0	31.41	0.835	0.403
0.9	31.88	0.841	0.362
0.99	32.09	0.844	0.326
0.999	32.22	0.851	0.296
0.9999	31.93	0.844	0.301
1	31.92	0.844	0.304

Table 5: Results of different decay rate η on DRealSR.

λ_1	PSNR \uparrow	SSIM \uparrow	LPIPS \downarrow
0	32.01	0.844	0.305
0.001	32.14	0.847	0.303
0.01	32.22	0.851	0.296
0.1	32.07	0.845	0.302

Table 6: Results of different λ_1 on DRealSR.

A.5. More Insights of Uncertainty Estimation

In fact, in addition to the uncertainty estimation (UE) method mentioned in the paper, we have tried two other

λ_2	PSNR \uparrow	SSIM \uparrow	LPIPS \downarrow
0	32.16	0.850	0.300
0.01	32.20	0.851	0.298
0.1	32.22	0.851	0.296
1	32.18	0.850	0.299

Table 7: Results of different λ_2 on DRealSR.

λ_3	PSNR \uparrow	SSIM \uparrow	LPIPS \downarrow
0	32.19	0.850	0.302
0.001	32.21	0.851	0.298
0.005	32.22	0.851	0.296
0.01	32.15	0.849	0.299
0.1	not converge	not converge	not converge

Table 8: Results of different λ_3 on DRealSR.

Batch Size	PSNR \uparrow	SSIM \uparrow	LPIPS \downarrow
16	32.20	0.851	0.297
32	32.22	0.851	0.296
64	32.22	0.851	0.297
128	32.19	0.850	0.298

Table 9: Results of different batch size on DRealSR.

approaches. In this section, we will present these two approaches and provide the corresponding experimental results.

Approach 1. In this approach, we do not replace the normalization function in the teacher model with Gumbel-Softmax [15]. Instead, after inputting the eight augmented LR images into the teacher model, we transform the resulting eight outputs back to their original geometry and compute their mean and variance. Then we compute the confidence map using Eq. (9).

Approach 2. In the second approach, the normalization function in the teacher model is replaced with Gumbel-Softmax. After getting eight SR images from the teacher model, we do not refine them into one pseudo-label but treat them as eight pseudo-labels. Then we repeat the above step N times and finally get $8 * N$ pseudo-labels. We transform them back to their original geometry and compute their mean and variance. Then we compute the confidence map using Eq. (9).

Method	PSNR \uparrow	SSIM \uparrow	LPIPS \downarrow
Approach 1	32.10	0.849	0.307
Approach 2	32.20	0.851	0.297
Ours	32.22	0.851	0.296
w/o UE	32.15	0.849	0.304

Table 10: Results of different UE methods on DRealSR.

As shown in Table. 10, the result with Approach 1 is even worse than without it. This may be attributed to inappropriate uncertainty estimation, which highlights the significance of Gumbel-Softmax for uncertainty estimation in the teacher model. Although Approach 2 also yields good results, it performs slightly inferior to our approach in terms of PSNR and LPIPS metrics, hence we do not adopt it. Furthermore, we provide additional visual illustrations of our UE method in Fig. 8. It can be found that pixels with higher error in pseudo-labels will be assigned lower confidence, which effectively rectifies inaccurate pseudo-labels.

A.6. Additional SR Visual Results

In order to further demonstrate the effectiveness of our method, we provide additional visual results on DRealSR [41] dataset. As shown in Fig. 9, without accessing source data, our method achieves more appealing visual results than other methods.

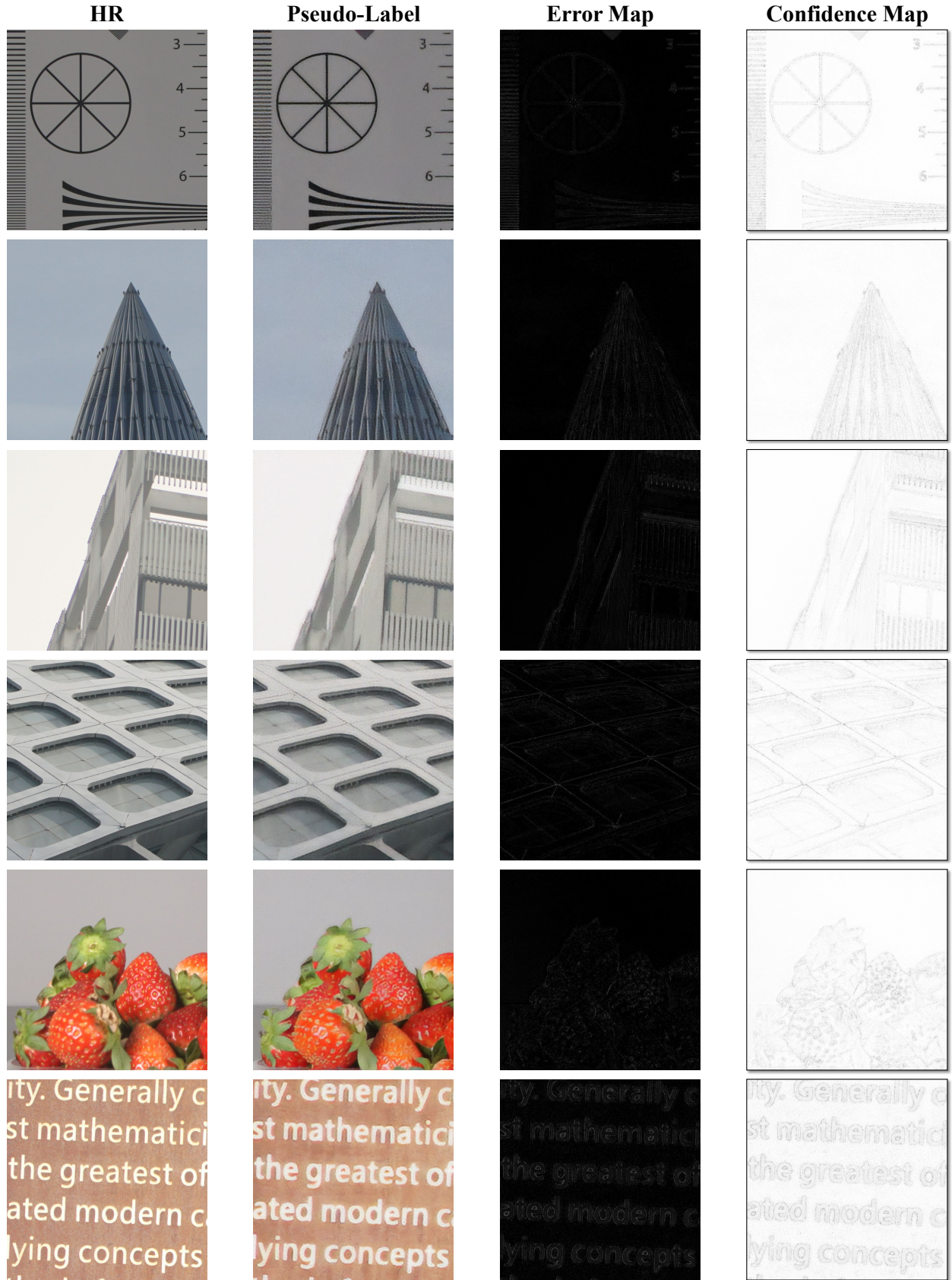


Figure 8: Visual illustrations of the uncertainty estimation. **Zoom in for best view.**



Figure 9: Visual results for $\times 4$ SR on DRealSR dataset (Sony \rightarrow Panasonic). **Zoom in for best view.**